Depth profiling of 3D skyrmion lattices in a chiral magnet—A story with a twist

Cite as: AIP Advances **11**, 015108 (2021); https://doi.org/10.1063/9.0000072
Submitted: 20 October 2020 . Accepted: 20 November 2020 . Published Online: 06 January 2021

G. van der Laan, S. L. Zhang, and T. Hesjedal

Depth profiling of 3D skyrmion lattices in a chiral magnet—A story with a twist

Cite as: AIP Advances 11, 015108 (2021); doi: 10.1063/9.0000072
Presented: 3 November 2019 • Submitted: 20 October 2020 •
Accepted: 20 November 2020 • Published Online: 6 January 2021

G. van der Laan,[1,a] S. L. Zhang,[2,3] and T. Hesjedal[2]

AFFILIATIONS

[1] Diamond Light Source, Harwell Science and Innovation Campus, Didcot, Oxfordshire OX11 0DE, United Kingdom
[2] Department of Physics, Clarendon Laboratory, University of Oxford, Oxford OX1 3PU, United Kingdom
[3] School of Physical Science and Technology, ShanghaiTech University, Shanghai 200031, China

Note: This paper was presented at the 65th Annual Conference on Magnetism and Magnetic Materials.
[a] **Author to whom correspondence should be addressed:** Gerrit.vanderLaan@diamond.ac.uk

ABSTRACT

From the perspective of surface science, only the topmost atomic layers usually exhibit physical properties that are different to those of the bulk material, whereas the deeper layers are assumed to be bulk-like and remain largely unexplored. Going beyond conventional diffraction and imaging techniques, we have determined the depth dependence of the full 3D spin structure of magnetic skyrmions below the surface of a bulk Cu_2OSeO_3 sample using the polarization dependence of resonant elastic x-ray scattering (REXS). While the bulk spin configuration showed the anticipated Bloch type structure, it was found that the skyrmion lattice changes to a Néel twisting (i.e., with a different helicity angle) at the surface within a distance of several hundred nm. The exact surface helicity angle and penetration length of this twist have been determined, revealing the detailed internal structure of the skyrmion tube. It was found that the experimental penetration length of the Néel twisting is 7× longer than the theoretical value given by the ratio of J/D. This indicates that apart from the considered spin interactions, i.e., the Heisenberg exchange interaction J and the Dzyaloshinskii-Moriya interaction D, as well as the Zeeman interaction, other effects must play an important role. The findings suggest that the surface reconstruction of the skyrmion lattice is a universal phenomenon, stemming from the breaking of translational symmetry at the interface.

I. INTRODUCTION

Traditionally, a sharp distinction is drawn between surface and bulk properties, and it is only seldom specified what happens further below the surface, and how deep the transition from surface to bulk properties extends below the surface. This limitation is mainly due to a lack of suitable experimental techniques. For instance, on the one hand, there are the typical magnetic surface probes, such as magnetic force microscopy and spin-polarized photoemission spectroscopy, and on the other hand, bulk sensitive probes, such as conventional magnetometry and polarized neutron scattering. Fortunately, soft x-rays from a synchrotron source with typical penetration depth of 100s of nm are able to bridge these two regions. Furthermore, soft x-rays offer the advantage of element-specificity, which in the case of multilayers converts into layer specificity. In this paper, we describe how the polarization dependence of resonant elastic x-ray scattering (REXS) can be used to probe the spin twisting of skyrmion tubes at depths of hundreds of nm below the surface.

Skyrmions are topologically nontrivial whirls of the magnetization which were theoretically proposed by Bogdanov *et al.*[1] They were experimentally observed by Mühlbauer *et al.* in the chiral magnet MnSi using small angle neutron scattering (SANS), where they form a hexagonal lattice with a periodicity of ~18 nm.[2] This was soon followed by real-space observation using Lorentz transmission electron microscopy (LTEM).[3] The well-defined spin topology in real space enables the magnetic skyrmions to many intriguing quantum mechanical phenomena including emergent electromagnetic dynamics,[4] effective magnetic monopole,[5] topological/skyrmion Hall effects.[6] Furthermore, due to their topological properties, magnetic skyrmions can behave as metastable quasiparticles and have been proposed as information carriers for ultralow power nonvolatile spintronics.[7,8]

II. SKYRMION ENERGETICS

The local energy density of a chiral lattice can be written as a hierarchy of the various energy scales,[2]

$$w = J\,(\nabla \mathbf{m})^2 + D\mathbf{m}\cdot(\nabla \times \mathbf{m}) - \mathbf{B}\cdot\mathbf{m}\,, \qquad (1)$$

with the first term being the strong isotropic exchange interaction with Heisenberg exchange constant J, which prefers a parallel spin alignment. The second term is the much weaker asymmetric exchange interaction, i.e., the Dzyaloshinskii-Moriya interaction (DMI) with scalar constant D, in $D_{ij}\cdot(s_i \times s_j)$, which prefers a perpendicular spin alignment. The DMI is due to the spin–orbit coupling (SOC) and is a consequence of the crystal structure (such as $P2_13$) which lacks inversion symmetry. The competition between both terms leads to a spin spiral with a pitch of $\lambda_h = 2\pi J/D$, which is ~60 nm for Cu_2OSeO_3. The third term is the Zeeman interaction, which aligns the spins along the applied field **B**. Other interactions omitted in Eq. (1) are the very weak crystal field effects (4^{th} order SOC) which pin the helix along symmetry directions of the crystal, and a term due to the demagnetization. Temperature fluctuations close to the transition temperature can stabilize the skyrmion phase. As the skyrmion lattice is only loosely bound to the crystal lattice, relatively small current densities can already induce motion of the skyrmion lattice.[9]

In the spin texture of a single skyrmion, each magnetic spin at a given position is characterized by two angles. The 2-spheres of the spin textures are shown by the *hedgehogs* in the upper part of Fig. 1(a,b). By mapping these spins and their orientations onto a sphere in order-parameter space, the topological key property—the winding number—can be determined. If each spin direction exists precisely once, the skyrmion has a winding number of $N = 1$.[10]

Here, we focus on skyrmions of Néel type (cycloidal spin texture; C_{nv} crystallographic class) and Bloch type (helical cycloidal spin texture; D_n). Other flavors are available as well, such as antiskyrmions with S_4 and D_{2d} symmetry.[11] For a Néel type texture [Fig. 1(a)] all spins are aligned along the radial direction of the sphere and the helicity angle is either $\chi = 0°$ or 180°. Combing the spins either clockwise (CW) or counterclockwise (CWW) results in a Bloch type texture [Fig. 1(b)], where at the equator the spins are tangential to the sphere ($\chi = \pm 90°$).

A stereographic projection brings the spin at the North Pole to the center of a 2D-plane, and the spin at the South Pole is mapped onto the boundary [Fig. 1(a,b)]. Due to the weak crystal field interaction, individual skyrmions in the 2D-plane combine into a lattice of hexagonal structure, extending into homogeneous skyrmion tubes in the third dimension [Fig. 1(c)].[12]

TABLE I. Properties of some skyrmion lattices, grouped by space group (SG). The values for the temperature range ΔT_c of the skyrmion phase and the wavelength λ_h of the helical phase are for guidance only as they vary across the literature.

SG	Material	ΔT_c (K)	λ_h (nm)	Conduction	Type
$P2_13$	MnSi	28-30	18	Metal	Bloch
	FeGe	273-280	70	Metal	Bloch
	$Fe_{1-x}Co_xSi$	2-50	30-230	Semicond.	Bloch
	$Mn_{1-x}Fe_xGe$	150-220	5-220	Metal	Bloch
	Cu_2OSeO_3	56-58	60-62	Insulator	Bloch
$P4_13$	$Co_xZn_yMn_z$	150-500	120-200	Metal	Bloch
$R3m$	GaV_4S_8	9-13	17-18	Semicond.	Néel
	GaV_4Se_8	18	19-24	Semicond.	Néel

Until recently, the skyrmion lattice was treated as a 2D object, extended into a 3D space without modulation along the z-direction, i.e., every single sheet of the skyrmion lattice was assumed to be identical. However, it was recently found that the solutions for skyrmions and helicoids *in thin layers* of cubic helimagnets are inhomogeneous along the film thickness.[14,15]

The question is what about *bulk crystals*, which can show a vast range of different properties, such as T_c and λ_h. Bulk skyrmion lattices in crystals with space group $P2_13$ and $P4_13$ are known to be Bloch type. On the other hand, those with space group $R3m$ are Néel type (see Table I).

The DMI is composed of Lifshitz invariants $\mathscr{L}_{ij}^{(k)} = m_i\partial m_j/\partial x_k - m_j\partial m_i/\partial x_k$, which depend on the magnetization components $m_{i(j)}$, in a specified crystal symmetry. Due to breaking of the translation symmetry at the surface, the DMI can be different from the bulk. Meynell *et al.*[14] reported chiral surface twists attributed to confined magnetic crystals lacking inversion symmetry. Rybakov *et al.*[15] presented a new type of thermodynamically stable magnetic state at interfaces and surfaces of chiral magnets, the so-called chiral bobbers.

In this paper, we demonstrate that by using the novel technique of circular dichroism (CD)-REXS we can determine the skyrmion helicity angle of bulk crystals, and thereby distinguish between Néel and Bloch type textures. Moreover, the probing depth dependence

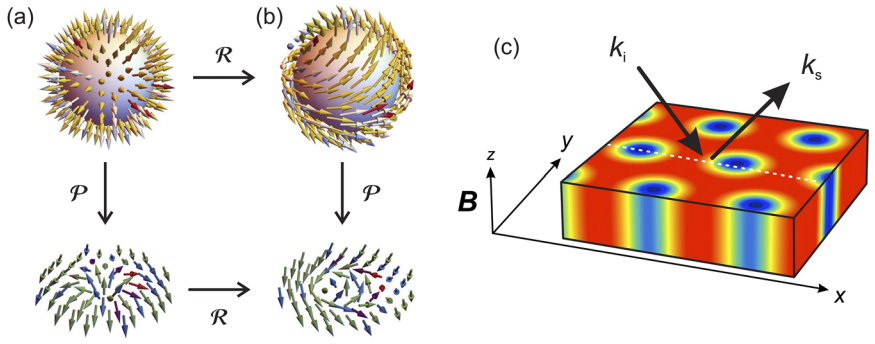

FIG. 1. Homotopic construction of 2D skyrmions with helicity angle χ. (a) Néel type ($\chi = 0°$, 180°). (b) Bloch type ($\chi = \pm 90°$). A 2D-skyrmion lattice with tubes along the third dimension. Panel (a,b) adapted from Kovalev and Sandhoefner, Front. Phys. 6, 98 (2018).[13] Copyright 2018 Authors, licensed under a Creative Commons Attribution CC BY 4.0. Panel (c) adapted from Zhang *et al.*, Nano Lett. 20, 1428 (2020)[12] with permission from the authors. Copyright 2020 Authors, licensed under a Creative Commons Attribution CC BY 4.0.

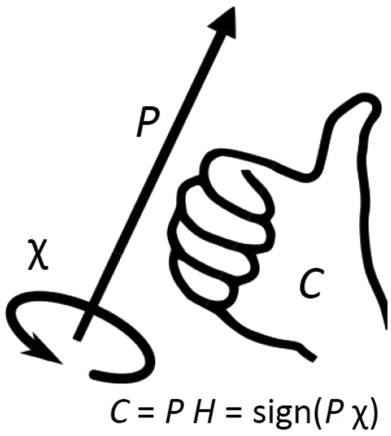

FIG. 2. Thumb rule giving the relation for the polarity P (vorticity), helicity angle χ, helicity H (rotation sense), and chirality C (handedness).

of the soft x-rays, which varies with photon energy across an absorption edge, allows us to obtain the variation of the helicity angle as a function of depth below the surface.

III. A THUMB RULE FOR CHIRALITY

When dealing with helicity aspects, it is useful to clarify the nomenclature, which can be borrowed from the description of vortices. For a vortex the *polarity* $P = +1(-1)$ for core spin parallel to $+z$ $(-z)$. The *helicity angle* $\chi = (-180^\circ, 0^\circ)$ for clockwise (CW) and $\chi = (0^\circ, +180^\circ)$ for counterclockwise rotation (CCW). The Bloch type textures have $\chi = \pm 90^\circ$ (chiral) and Néel type textures have $\chi = 0^\circ, 180^\circ$ (i.e., they are achiral). Further, the *helicity* (rotation sense) is defined as $H = \mathrm{sgn}(\chi)$. The product of P and H determines the *chirality* (handedness) as $C = PH = \mathrm{sign}(P\chi)$. This can be either right-handed $(C = +1)$ or left-handed $(C = -1)$, see Fig. 2. Note that C is conserved under magnetic field reversal. For skyrmions, the chirality is determined by the sign of the DMI.

IV. MODELING OF THE MODIFIED SURFACE SKYRMION STRUCTURE

To investigate theoretically the stability of surface twisting, we used the local energy density w given in Eq. (1), assuming that the skyrmions in the bulk are Bloch type. The top layer at the surface $(z{=}0)$ then has a helicity angle $\chi(0) = \chi_0 + 90^\circ$, and the decay length of the helicity angle is L_p. This gives the ansatz for the helicity angle $\chi(z)$ as a function of depth z as follows:

$$\chi(z) = \chi_0 e^{-z/L_p} - C \times 90^\circ. \tag{2}$$

Micromagnetic modeling for bulk Cu_2OSeO_3 (001) gave the $\chi(z)$ profile with the lowest energy for $L_p = 7.1$ nm and $\chi(0) = -134^\circ$.[16]

Instead, we can also use a more heuristic approach. Theoretically, the helicity angle decay length, which is proportional to the helix wavelength, is $L_{\mathrm{th}} = J/D$. For Cu_2OSeO_3 this gives $L_{\mathrm{th}} \approx J/D \approx \lambda_h/2\pi \approx 9.5$ nm.[17]

V. RESONANT ELASTIC X-RAY SCATTERING

A. Experimental

Our REXS measurements were carried out in the UHV soft x-ray diffractometer RASOR on beamline I10 at the Diamond Light Source. This diffractometer is equipped with a CCD camera, liquid He cryostat, and variable magnetic field that can be tilted by an

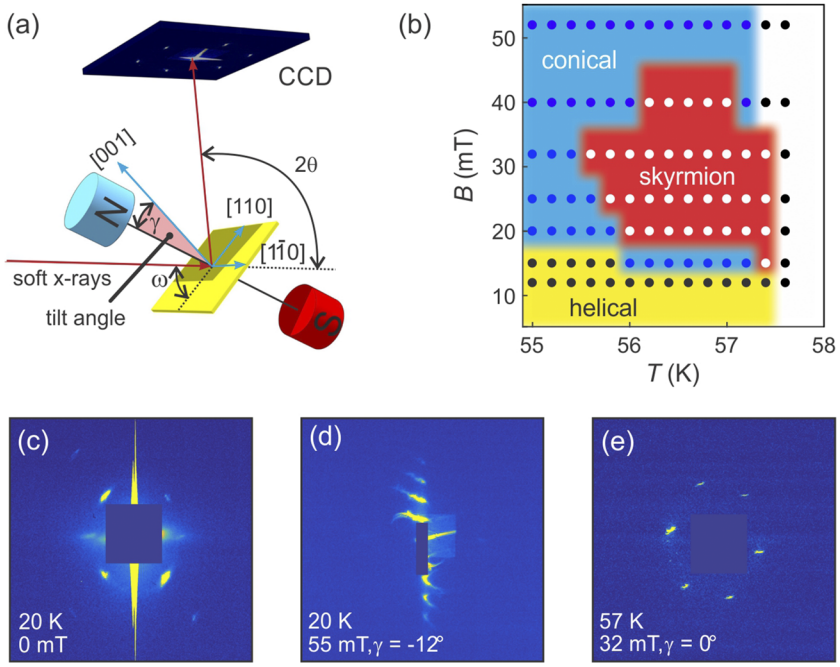

FIG. 3. Typical REXS data for the different magnetic phases in Cu_2OSeO_3. (a) REXS set-up in RASOR. (b) *B-T* phase diagram. CCD image showing the reciprocal space map of *hk* plane for (c) helical state (twinned), (d) conical state, and (e) sixfold skyrmion lattice state. Reprinted (adapted) with permission from Zhang *et al.*, Nano Lett. 16, 3285 (2016).[18] Copyright (2016) American Chemical Society.

angle γ, as shown in the setup in Fig. 3(a). The magnetic field is supplied by two permanent magnets which can be positioned to vary the field strength and orientation within the scattering plane. Figure 1(b) shows the scattering plane (x-y) containing incident and scattered beam with wavevector $\mathbf{k}_i$ and $\mathbf{k}_s$, respectively, and polarization ε_i and ε_s. The field is along the skyrmion tubes.

Figure 3(b) shows the (B-T) phase diagram for Cu_2OSeO_3 (001) near the vicinity of the skyrmion pocket measured by REXS at the Cu L_3 edge.[18,19] At temperatures below ~57 K in zero field, the lattice is in the helical phase showing in total four magnetic peaks in the diffraction pattern around the (001) reflection, due to twin domains [Fig. 3(c)]. Increasing the B-field, Cu_2OSeO_3 goes over to the conical phase with the diffraction pattern shown in Fig. 3(d). A further increase in field gives the field polarized state, with no magnetic diffraction peaks. Between ~56-57 K and ~20-45 mT, the skyrmion lattice pocket is found [Fig. 3(e)], which gives a six-fold pattern due to the hexagonal skyrmion lattice [Fig. 1(c)]. It is weakly linked to the atomic lattice structure, so that an azimuthal rotation of the crystal equally gives a rotation of the six-fold magnetic satellites.

B. Theory

The Cu $L_{2,3}$ REXS arises from the virtual transition between the Cu $2p$ core level and the $3d$ valence states. At the energy of the $L_{2,3}$ resonance, the scattering cross section becomes sensitive to the magnetic polarization of the $3d$ states, which gives a difference in transition probability for left- and right-circularly polarized x-rays, resulting in circular dichroism. In the electric-dipole approximation, the diffracted intensity $I(\mathbf{Q})$ for a scattering vector $\mathbf{Q} = \mathbf{k}_s - \mathbf{k}_i$ is

$$I(\boldsymbol{\omega}, \mathbf{Q}) \propto |\sum_j f_j(\omega) \exp(i\mathbf{Q}\cdot\mathbf{r}_j)|^2, \tag{3}$$

where the summation runs over all sites j. Taking

$$F_n\mathbf{M}(\mathbf{Q}) = \int d\mathbf{r}^2 f_n \mathbf{m}(\mathbf{r}) e^{i\mathbf{Q}\cdot\mathbf{r}}, \tag{4}$$

where F_n is the Fourier transform of f_n (for n = 0, 1, 2 as explained below), and $\mathbf{M}(\mathbf{Q})$ is the Fourier transform of the real-space magnetization configuration $\mathbf{m}(\mathbf{r})$, Eq. (3) can be written as[20]

$$\mathcal{F}(\mathbf{Q}) = F_0\overline{\rho}(\hat{\varepsilon}_s^*\cdot\hat{\varepsilon}_i) - iF_1(\hat{\varepsilon}_s^*\times\hat{\varepsilon}_i)\cdot\mathbf{M} + F_2(\hat{\varepsilon}_s^*\cdot\mathbf{M})(\hat{\varepsilon}_i\cdot\mathbf{M}). \tag{5}$$

The first term with F_0 gives the Thomson scattering arising from the charge density, the second term with F_1 gives the linear magnetic contribution, and the third term with F_2 gives the quadratic magnetic contribution, which is often small and therefore neglected. The chiral lattice is incommensurate with the electron density so that the charge-magnetic interference term F_0F_1 vanishes in $|\mathcal{F}|^2$, leaving only the pure magnetic term proportional to $|F_1|^2$.

Using the 2×2 density matrix μ for the light polarization

$$\mu = \frac{1}{2}(P_0\sigma_0 + \mathbf{P}\cdot\sigma) = \frac{1}{2}\begin{pmatrix} P_0+P_1 & P_2 - iP_3 \\ P_2 + iP_3 & P_0 - P_1 \end{pmatrix}, \tag{6}$$

where σ are the Pauli matrices, and $\mathbf{P}$ is the Poincaré-Stokes representation of the light polarization, we obtain the scattering cross section $I(\mathbf{Q})$ by summing over all scattered light polarizations, by taking the trace[20]

$$I(\mathbf{Q}) = \mathrm{Tr}[\mathcal{F}\cdot\mu\cdot\mathcal{F}^\dagger]. \tag{7}$$

For circularly polarized light, with $P_0 = 1$, $P_1 = P_2 = 0$, $P_3 = \pm 1$, we obtain[20]

$$I_{\mathrm{CD}}(\mathbf{Q}) = 2|F_1|^2\mathrm{Im}\{[\mathbf{k}_s\cdot\mathbf{M}^*(\mathbf{Q})](\mathbf{k}_s\times\mathbf{k}_i)\cdot\ \mathbf{M}(\mathbf{Q})\}. \tag{8}$$

Applying this result to the angular texture of the skyrmion in the 2D plane [see Fig. 1(a,b)] gives for the circular dichroism (CD) of the magnetic scattering peaks

$$I_{\mathrm{CD}}(\Psi) \propto |F_1|^2\ \sin(\Psi + \chi), \tag{9}$$

where Ψ is the azimuthal angle with respect to the scattering plane (z-x plane) and χ is the helicity angle of skyrmion lattice.[19] For a Néel texture ($\chi = 0^\circ$ or 180°) this gives $I_{\mathrm{CD}} \propto \sin\Psi$ so that the CD signal is extinct along the scattering plane, and maximal normal to it [Fig. 4(a)]. In contrast, for a Bloch texture the CD is extinct normal to the scattering plane, and maximal along it [Fig. 4(d)]. Of course, intermediate orientations can also be directly identified. Figure 4 displays the hedgehog structure and projected spin texture together with the associated calculated diffraction pattern, where the color bar represents the dichroic intensity. Thus, there is a one-to-one

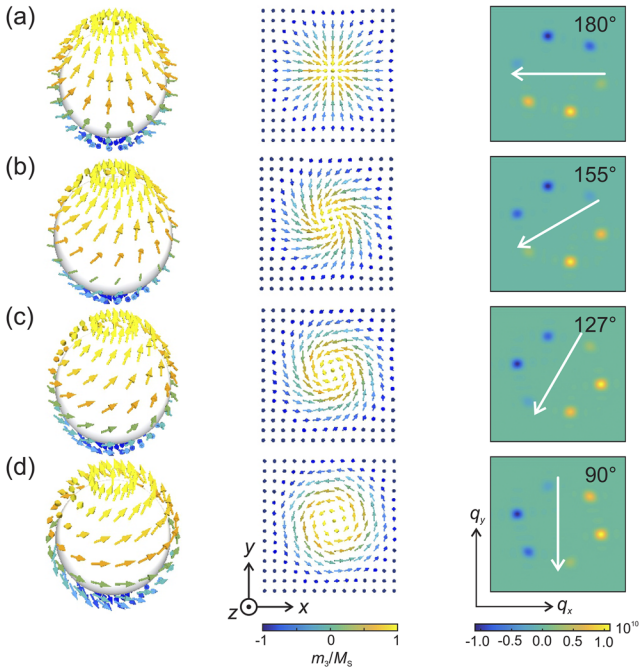

FIG. 4. Illustration of the skyrmion order for different helicity angles on the surface of a sphere for skyrmions with winding number N=1 varying between (a) Néel, (b,c) intermediate, and (d) Bloch twisting. The hedgehog configurations (left column) are connected by stereographic projection to the real-space planar configurations (middle column). The calculated CD-REXS diffraction pattern (right column) associated with a hexagonal lattice composed of the spin configurations in the middle. The scattering is in the x-z plane. The direction of the extinction line (white arrow) corresponds to the helicity angle χ denoted on the right-hand panels. Consequently, the chirality of the skyrmions can be straightforwardly determined). $\chi = 180^\circ$ and $\chi = 90^\circ$ correspond to pure Néel and pure Bloch-twisting, respectively. Figure adapted from S. L. Zhang *et al.*, PNAS 115, 6386 (2018).[17]

relation between the helicity angle and its CD-REXS pattern. The direction of dichroism extinction, indicated by the white arrows in the diffraction patterns, can be determined most accurately by fitting the CD intensities of the magnetic satellites across the azimuth using a sine function. It is important to note that this not only holds for an ordered skyrmion lattice, but also for a disordered lattice, e.g., a multi-domain state.[21] In this case, the diffraction image displays a necklace-like or ring pattern, but the dichroism within the diffraction circle still obeys the dependence given by Eq. (9).[16] This is because, while the crystal lattice is orientation dependent, the spin texture of each skyrmion is invariant for azimuthal rotations. Hence, Eq. (9) offers us a universal *dichroism extinction rule* (DER) to determine the helicity angle.[22] Recently, this method was also used to study the spin textures of skyrmions in magnetic multilayers, such as $[\mathrm{Ta/CoFeB/MgO}]_n$,[23] $[\mathrm{Ir/Co/Pt}]_n$,[24] and $[\mathrm{Pt/Co/AlO}_x]_n$.[25]

VI. DEPTH DEPENDENCE OF REXS

Since the x-ray scattering has a finite sampling depth, we have to take the weighted average over all 2D planes that are probed by REXS.

In a material with an energy dependent absorption coefficient $\mu(\omega)$, the x-ray flux that reaches a layer at depth z decreases as $\exp[-z\mu(\omega)/\cos\alpha]$, where α is the angle of incident x-rays with respect to the surface normal.[26,27] The x-ray attenuation length is $\Lambda(\omega) = \mu^{-1}(\omega)$ which is 98 nm for Cu_2OSeO_3 at the Cu L_3 maximum (933.5 eV). Taking $I(\Psi, z)$ as the signal from the layer z, the total intensity is

$$I_{\mathrm{CD}}^{\mathrm{total}}(\Psi) = \int_0^\infty I_{\mathrm{CD}}(\Psi, z)\, Y(z) dz. \tag{10}$$

Taking the scattering angle equal in magnitude to the incident angle, the attenuation function is

$$Y(z) = \frac{1}{\Lambda(\omega)} \exp\left(-\frac{2z}{\Lambda(\omega)} \sec\alpha\right), \tag{11}$$

where ω is the photon energy. Therefore the effective x-ray sampling depth d_a is

$$d_a(\omega) = \frac{1}{2}\Lambda(\omega)\cos\alpha. \tag{12}$$

The minimum value of d_a = 34.6 nm for Cu_2OSeO_3 is obtained at the maximum of the Cu L_3 absorption edge. Off edge, d_a increases to ~100 nm. The energy dependence of the x-ray sampling depth d_a across the Cu $L_{2,3}$ edge under diffraction condition in Cu_2OSeO_3 is shown in Fig. 5(a). If the helicity angle decay length L_p is small, or on the order of Λ, we can use the depth dependent probing of REXS across the absorption edge.

Figure 5(b) shows the helicity angle χ taken directly from the measured CD-REXS diffraction pattern, as obtained using the DER on the CD-REXS pattern. Figure 5(c) and 5(d) show typical experimental REXS intensity patterns obtained at photon energies of 931.25 eV (at the edge) and 932.45 eV (above the edge). The white arrows give the extinction direction. For comparison, Fig. 5(e) and 5(f) show the calculated REXS intensity pattern based on the intensity attenuation. The variation in the helicity angle is compared in Fig. 5(b) with a fit to the depth dependence (red line), which confirms the direct relation between χ and d_a. The CD-REXS measurements show that the Néel twisting at the surface penetrates deep into the bulk and turns into pure Bloch twisting at 62 nm ($1/e$ decay). A qualitative picture is seen in Fig. 4, showing the gradual transition from Néel type at the top to Bloch type deeper down.

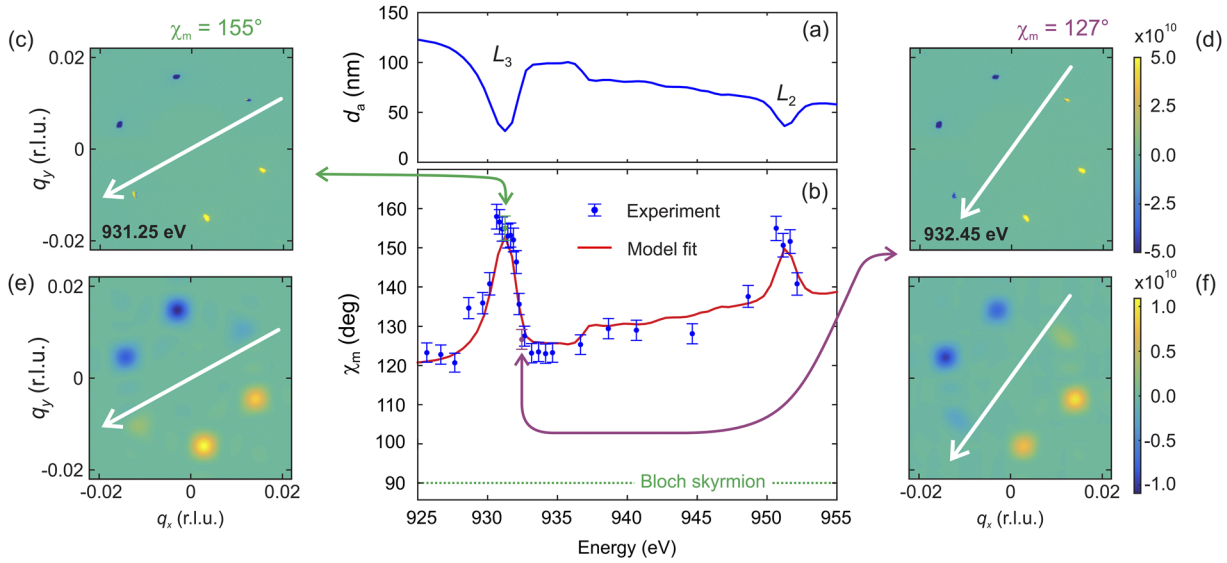

FIG. 5. (a) Energy dependence of the x-ray sampling depth d_a across the Cu $L_{2,3}$ edge under diffraction condition in Cu_2OSeO_3 (001). (b) Helicity angle χ taken directly from the measured CD-REXS diffraction pattern. (c,d) Typical experimental REXS intensity patterns observed at photon energies of 931.25 eV (at the edge) and 932.45 eV (above the edge). The extinction direction is shown by the white arrows. Figure adapted from S. L. Zhang *et al.*, PNAS 115, 6386 (2018).[17]

This leaves us with one final twist in the knickers, namely that the experimentally observed decay length of the helicity angle is ~ 7× longer than the theory value of J/D. This suggests that apart from J and D, there must be other interactions playing a role, such as magnon (spin wave) softening at the surface.[28] The DMI imposes boundary conditions on the magnetization which result in a reconstruction of the magnetization profile close to surfaces. For the field polarized state this just translates to a twist of the magnetization along, or perpendicular to, the surface normal depending on the type of DMI. This surface twist can act as an attractive potential on the spin wave excitations leading to magnon modes that are bound to the edge of the sample.[29]

VII. CONCLUSIONS

We have demonstrated that CD-REXS unambiguously measures the helicity angle of skyrmions near the surface by using the universal *dichroism extinction rule* (DER).[22] The depth dependence is obtained by tuning the photon energy across the absorption edge.[16,17] It was found that Néel twisting at the surface penetrates deep into the bulk and turns into pure Bloch twisting over a $(1/e)$ lengthscale of 62 nm. This is larger than the theoretically predicted value, which we ascribe to magnon softening at the surface.

Skyrmion surface twisting is a universal phenomenon, stemming from the translation symmetry breaking at the surface (or interface). The helicity angle χ gives an additional degree of freedom of the skyrmion, which may be further exploited for applications.

Moreover, the technique of CD-REXS is well suited for probing the magnetization dynamics, which has become an important contemporary topic of research. Very recently it was demonstrated that soft x-ray diffraction[30] and reflectivity[31] can be combined with x-ray detected ferromagnetic resonance,[32] providing depth sensitive information of the magnetization dynamics in the GHz range of magnetic multilayers. This technique exploits the stroboscopic probing using the time structure of the synchrotron pulses. Even shorter time scales would be possible using x-ray free electron lasers.

ACKNOWLEDGMENTS

S. L. Z. and T. H. acknowledge financial support by EPSRC (EP/N032128/1). Experiments were carried out on beamline I10 at the Diamond Light Source, UK, under proposals SI-11784, SI-12943, and SI-12958.

DATA AVAILABILITY

Data sharing is not applicable to this article as no new data were created or analyzed in this study.

REFERENCES

[1] A. N. Bogdanov and D. A. Yablonskii, Zh. Eksp. Teor. Fiz. **95**, 178 (1989).
[2] S. Mühlbauer, B. Binz, F. Jonietz, C. Pfleiderer, A. Rosch, A. Neubauer, R. Georgii, and P. Böni, Science **323**, 915 (2009).
[3] X. Z. Yu, Y. Onose, N. Kanazawa, J. H. Park, J. H. Han, Y. Matsui, N. Nagaosa, and Y. Tokura, Nature **465**, 901 (2010).
[4] T. Schulz, R. Ritz, A. Bauer, M. Halder, M. Wagner, C. Franz, C. Pfleiderer, K. Everschor, M. Garst, and A. Rosch, Nat. Phys. **8**, 301 (2012).
[5] P. Milde, D. Kohler, J. Seidel, L. M. Eng, A. Bauer, A. Chacon, J. Kindervater, S. Muhlbauer, C. Pfleiderer, S. Buhrandt, C. Schutte, and A. Rosch, Science **340**, 1076 (2013).
[6] A. Neubauer, C. Pfleiderer, B. Binz, A. Rosch, R. Ritz, P. G. Niklowitz, and P. Boni, Phys. Rev. Lett. **102**, 186602 (2009).
[7] A. Hoffmann and S. D. Bader, Phys. Rev. Appl. **4**, 047001 (2015).
[8] S. L. Zhang, W. W. Wang, D. M. Burn, H. Peng, H. Berger, A. Bauer, C. Pfleiderer, G. van der Laan, and T. Hesjedal, Nat. Commun. **9**, 2115 (2018).
[9] X. Z. Yu, N. Kanazawa, W. Z. Zhang, T. Nagai, T. Hara, K. Kimoto, Y. Matsui, Y. Onose, and Y. Tokura, Nat. Commun. **3**, 988 (2012).
[10] S. L. Zhang, G. van der Laan, and T. Hesjedal, Nat. Commun. **8**, 14619 (2017).
[11] A. O. Leonov, T. L. Monchesky, N. Romming, A. Kubetzka, A. N. Bogdanov, and R. Wiesendanger, New J. Phys. **18**, 065003 (2016).
[12] S. L. Zhang, D. M. Burn, N. Jaouen, J.-Y. Chauleau, A. A. Haghighirad, Y. Liu, W. W. Wang, G. van der Laan, and T. Hesjedal, Nano Lett **20**, 1428 (2020).
[13] A. A. Kovalev and S. Sandhoefner, Front. Phys. **6**, 98 (2018).
[14] S. A. Meynell, M. N. Wilson, H. Fritzsche, A. N. Bogdanov, and T. L. Monchesky, Phys. Rev. B **90**, 014406 (2014).
[15] F. N. Rybakov, A. B. Borisov, S. Blügel, and N. S. Kiselev, Phys. Rev. Lett. **115**, 117201 (2015).
[16] S. L. Zhang, G. van der Laan, W. W. Wang, A. A. Haghighirad, and T. Hesjedal, Phys. Rev. Lett. **120**, 227202 (2018).
[17] S. L. Zhang, G. van der Laan, J. Müller, L. Heinen, M. Garst, A. Bauer, H. Berger, C. Pfleiderer, and T. Hesjedal, Proc. Natl. Acad. Sci. U.S.A. (PNAS) **115**, 6386 (2018).
[18] S. L. Zhang, A. Bauer, D. M. Burn, P. Milde, E. Neuber, L. M. Eng, H. Berger, C. Pfleiderer, G. van der Laan, and T. Hesjedal, Nano Lett. **16**, 3285 (2016).
[19] S. L. Zhang, A. Bauer, H. Berger, C. Pfleiderer, G. van der Laan, and T. Hesjedal, Phys. Rev. B **93**, 214420 (2016).
[20] G. van der Laan, C. R. Phys **9**, 570 (2008).
[21] S. L. Zhang, A. Bauer, H. Berger, C. Pfleiderer, G. van der Laan, and T. Hesjedal, Appl. Phys. Lett. **109**, 192406 (2016).
[22] S. L. Zhang, G. van der Laan, and T. Hesjedal, Phys. Rev. B **96**, 094401 (2017).
[23] W. Li, I. Bykova, S. Zhang, G. Yu, R. Tomasello, M. Carpentieri, Y. Liu, Y. Guang, J. Gräfe, M. Weigand, G. v. Laan, T. Hesjedal, C. Wan, J. Feng, X. Wang, C. Guo, G. Finocchio, X. Han, and G. Schütz, Adv. Mater. **31**, 1807683 (2019).
[24] J.-Y. Chauleau, W. Legrand, N. Reyren, D. Maccariello, S. Collin, H. Popescu, K. Bouzehouane, V. Cros, N. Jaouen, and A. Fert, Phys. Rev. Lett. **120**, 037202 (2018).
[25] W. Legrand, J.-Y. Chauleau, D. Maccariello, N. Reyren, S. Collin, K. Bouzehouane, N. Jaouen, V. Cros, and A. Fert, Sci. Adv. **4**, eaat0415 (2018).
[26] G. van der Laan and B. T. Thole, J. Electron Spectrosc. Relat. Phenom. **46**, 123 (1988).
[27] G. van der Laan and A. I. Figueroa, Coord. Chem. Rev. **277-278**, 95 (2014).
[28] R. Georgii and T. Weber, Quantum Beam Sci **3**, 4 (2019).
[29] J. Müller, A. Rosch, and M. Garst, New J. Phys. **18**, 065006 (2016).
[30] D. M. Burn, S. L. Zhang, K. Zhai, Y. Chai, Y. Sun, G. van der Laan, and T. Hesjedal, Nano Lett. **20**, 345 (2020).
[31] D. M. Burn, S. L. Zhang, G. Q. Yu, Y. Guang, H. J. Chen, X. P. Qiu, G. van der Laan, and T. Hesjedal, Phys. Rev. Lett. **125**, 137201 (2020).
[32] G. van der Laan, J. Electron Spectrosc. Relat. Phenom. **220**, 137 (2017).